JBC RESEARCH ARTICLE

Conformational interdomain flexibility in a bacterial α-isopropylmalate synthase is necessary for leucine biosynthesis

Received for publication, September 29, 2022, and in revised form, December 1, 2022 Published, Papers in Press, December 9, 2022,
https://doi.org/10.1016/j.jbc.2022.102789

Yu Bai[1,2,‡], **Wanting Jiao**[1,2,‡], **Jan Vörster**[3], **and Emily J. Parker**[1,2,*]

From the [1]*Ferrier Research Institute, Victoria University of Wellington, Wellington, New Zealand;* [2]*Maurice Wilkins Centre for Molecular Biodiscovery, Auckland, New Zealand;* [3]*School of Chemical and Physical Sciences, Victoria University of Wellington, Wellington, New Zealand*

Edited by Wolfgang Peti

α-Isopropylmalate synthase (IPMS) catalyzes the first step in leucine (Leu) biosynthesis and is allosterically regulated by the pathway end product, Leu. IPMS is a dimeric enzyme with each chain consisting of catalytic, accessory, and regulatory domains, with the accessory and regulatory domains of each chain sitting adjacent to the catalytic domain of the other chain. The IPMS crystal structure shows significant asymmetry because of different relative domain conformations in each chain. Owing to the challenges posed by the dynamic and asymmetric structures of IPMS enzymes, the molecular details of their catalytic and allosteric mechanisms are not fully understood. In this study, we have investigated the allosteric feedback mechanism of the IPMS enzyme from the bacterium that causes meningitis, *Neisseria meningitidis* (*Nme*IPMS). By combining molecular dynamics simulations with small-angle X-ray scattering, mutagenesis, and heterodimer generation, we demonstrate that Leu-bound *Nme*IPMS is in a rigid conformational state stabilized by asymmetric interdomain polar interactions. Furthermore, we found removing these polar interactions by mutagenesis impaired the allosteric response without compromising Leu binding. Our results suggest that the allosteric inhibition of *Nme*IPMS is achieved by restricting the flexibility of the accessory and regulatory domains, demonstrating that significant conformational flexibility is required for catalysis.

Enzyme catalysis is a structurally dynamic process consisting of multiple steps including substrate binding, transition state stabilization, and product release (1–4). The activity of an enzyme can be regulated by allostery, which effectively tunes catalysis by ligand-binding remote to the active site. Allostery occurs *via* altering the accessible dynamic conformational landscape of the enzyme, which is often associated with either conformational changes or subtle dynamic changes (4–10). Allostery plays a crucial role in the regulation of many biosynthetic pathways (11–15). In these cases, some allosterically controlled enzymes adopt multidomain assemblies so that the allosteric signal must be transmitted between catalytic and regulatory domains (15–19). Because of the versatile and complicated structural and biochemical characteristics of multidomain enzymes, the understanding of the molecular underpinnings of crossdomain allosteric communication is limited.

α-Isopropylmalate synthase (IPMS) catalyzes the reaction between acetyl-coenzyme A (AcCoA) and α-ketoisovalerate (α-KIV) to produce CoA and α-isopropylmalate, in the first committed step in the biosynthesis of the amino acid leucine (Leu). The catalytic activity of IPMS is allosterically inhibited by the pathway end product Leu (20, 21). Crystal structures of IPMS from *Mycobacterium tuberculosis* (*Mtu*IPMS) reveal a homodimeric quaternary structure. Each protomer contains an N-terminal TIM-barrel catalytic domain and a C-terminal regulatory domain that hosts the Leu-binding site. The catalytic and regulatory domains are connected by an accessory domain that is divided into two parts, subdomains I and II (Fig. 1*A*) (22, 23). The homodimer adopts a domain-swapped arrangement, with the accessory and regulatory domains from one monomer interacting with the catalytic domain of the other monomer (Fig. 1*A*) (23). The crystal structures of *Mtu*IPMS show marked asymmetry because of different positions adopted by the accessory and regulatory domains relative to the catalytic domain. Superimposition of the two chains at the catalytic domain showed a distance of 62.3 Å between the center of mass of the two regulatory domains (d_{reg}) (Fig. 1*B*). One of the active sites is capped by the accessory domain of the other chain and can be described as in a "closed" conformation (Fig. 1*C*), whereas the other active site is in the "open" conformation with the accessory subdomain II and the regulatory domain positioned at the side of the catalytic domain (Fig. 1*C*).

Previous studies have revealed that the accessory domain is essential to the catalytic activities of IPMS enzymes. Catalytic activity was significantly impaired in truncated forms of *Mtu*IPMS, IPMS from *Neisseria meningitidis* (*Nme*IPMS) (16, 22), and for the IPMS isoenzymes from *Leptospira biflexa* (*Lbi*IPMS1 and *Lbi*IPMS2) that lack the regulatory domain and

‡ These authors contributed equally to this work.
* For correspondence: Emily J. Parker, emily.parker@vuw.ac.nz.
Present address for Yu Bai: Institute of Microbiology, Anhui Academy of Medical Sciences, Hefei, China.

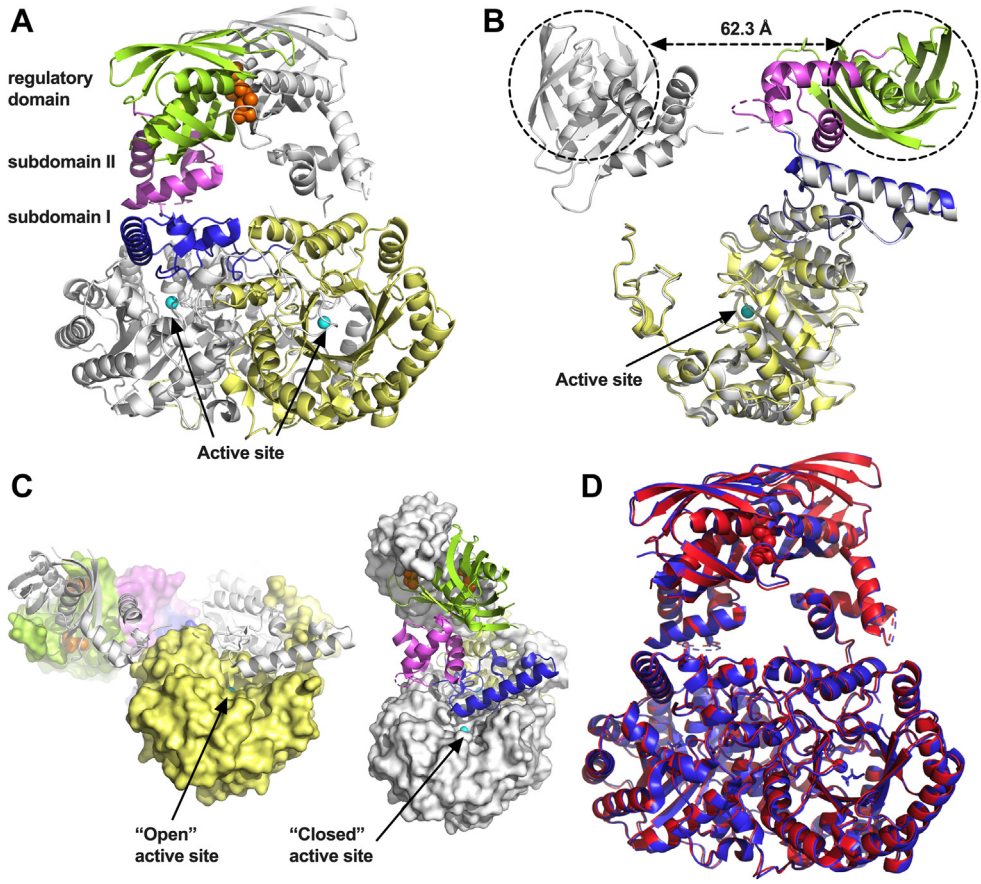

Figure 1. The crystal structure of *Mtu*IPMS shows an asymmetric homodimer. *A*, asymmetric domain–swapped dimer of *Mtu*IPMS with Leu bound (Protein Data Bank ID: 3FIG). Chain A is shown in *white*, chain B is colored to show the constituting domains, including catalytic domain (*yellow*), subdomain I (*blue*), and subdomain II (*pink*) of the accessory domain and the regulatory domain (*green*). Leu bound in the allosteric sites is displayed as *orange spheres*. The active site metal ion (Zn^{2+}) is shown as a *cyan sphere*. *B*, superimposition of the two chains at the catalytic domain reveals large conformational differences. Distance between the center of mass of the two regulatory domain is 62.3 Å. Location of the active site is indicated by the Zn^{2+} ion shown as a *cyan sphere*. *C*, the "open" active site with the accessory and regulator domains positioned at the side of the catalytic barrel and the "closed" active site with the accessory and regulatory domains capping the top of the catalytic barrel. The protein chain containing the "closed" or "open" active site is shown in surface representations, and the other protein chain is displayed as *cartoons*. Chain color scheme is maintained the same as that used in (*A*). *D*, superimposition between the α-KIV bound *Mtu*IPMS (Protein Data Bank ID: 1SR9, *blue*) and Leu-bound *Mtu*IPMS (PDB ID: 3FIG, *red*). α-KIV, α-ketoisovalerate; *Mtu*IPMS, IPMS from *Mycobacterium tuberculosis*.

part of the accessory domain (24). The accessory domain was also shown to contribute to the allosteric regulation of IPMS. Amino acid substitution of residues from subdomain I (His379 or Tyr410) and II (Asp444) showed disrupted allosteric response to Leu in *Mtu*IPMS (25, 26). Despite the lack of notable conformational changes between α-KIV-bound or Leu-bound *Mtu*IPMS crystal structures (Fig. 1*D*), solution-phase amide hydrogen/deuterium exchange experiments revealed a decreased deuterium incorporation percentage of residues 453 to 457 in subdomain II associated with Leu binding, which indicated a shift in conformational equilibria of this region (27).

The dynamic and asymmetric structures of IPMS enzymes pose a challenge for the study of the molecular detail in their catalytic and allosteric mechanisms. Consequently, the role of the accessory domain in propagating the allosteric signals and the contribution the structural asymmetry makes to catalysis and allostery in IPMS is unclear. In this study, we have conducted molecular dynamics (MD) simulations to explore the changes in domain dynamics and identify interdomain polar contacts important for the allosteric mechanism in *Nme*IPMS. Variant enzymes that contain amino acid substitutions in either one or both chains of the homodimer were generated and characterized structurally and biochemically to verify the role of the accessory domain and asymmetry in the allosteric mechanism of *Nme*IPMS. Our findings reveal that allosteric inhibition of *Nme*IPMS by Leu is effected by locking the enzyme in a rigid conformational state stabilized by asymmetric interdomain polar interactions.

Results

Leu binding is associated with changing conformational dynamics of the accessory domains of Nme*IPMS*

To investigate the changes in the conformational dynamics of *Nme*IPMS associated with allostery, we conducted MD simulations for ligand-free, KIV-bound, and Leu-bound *Nme*IPMS. Three replicates of MD simulations were

conducted for each system, and the equilibrated periods from the MD simulations were analyzed.

All MD simulations started from the same asymmetric conformation as observed in the crystal structure of *Mtu*IPMS (Protein Data Bank [PDB] ID: 1SR9). The active site of chain A is in the open conformation, and the active site of chain B is capped by the accessory domain of chain A and is in a closed conformation. While all three systems (ligand-free, KIV-bound, and Leu-bound *Nme*IPMS) remained in an asymmetric dimer conformation during the MD simulations, subtle differences were observed in the positions of the accessory and regulatory domains between the ligand-bound and ligand-free systems; the KIV-bound *Nme*IPMS sampled slightly less asymmetric conformations (d_{reg} = 80 ± 5.0 Å) than Leu-bound *Nme*IPMS (d_{reg} = 94 ± 6.0 Å) (Table S1). MD average structures of KIV-bound and ligand-free *Nme*IPMS, when aligned at the catalytic domains, showed that the accessory domain of chain A was placed further away from the

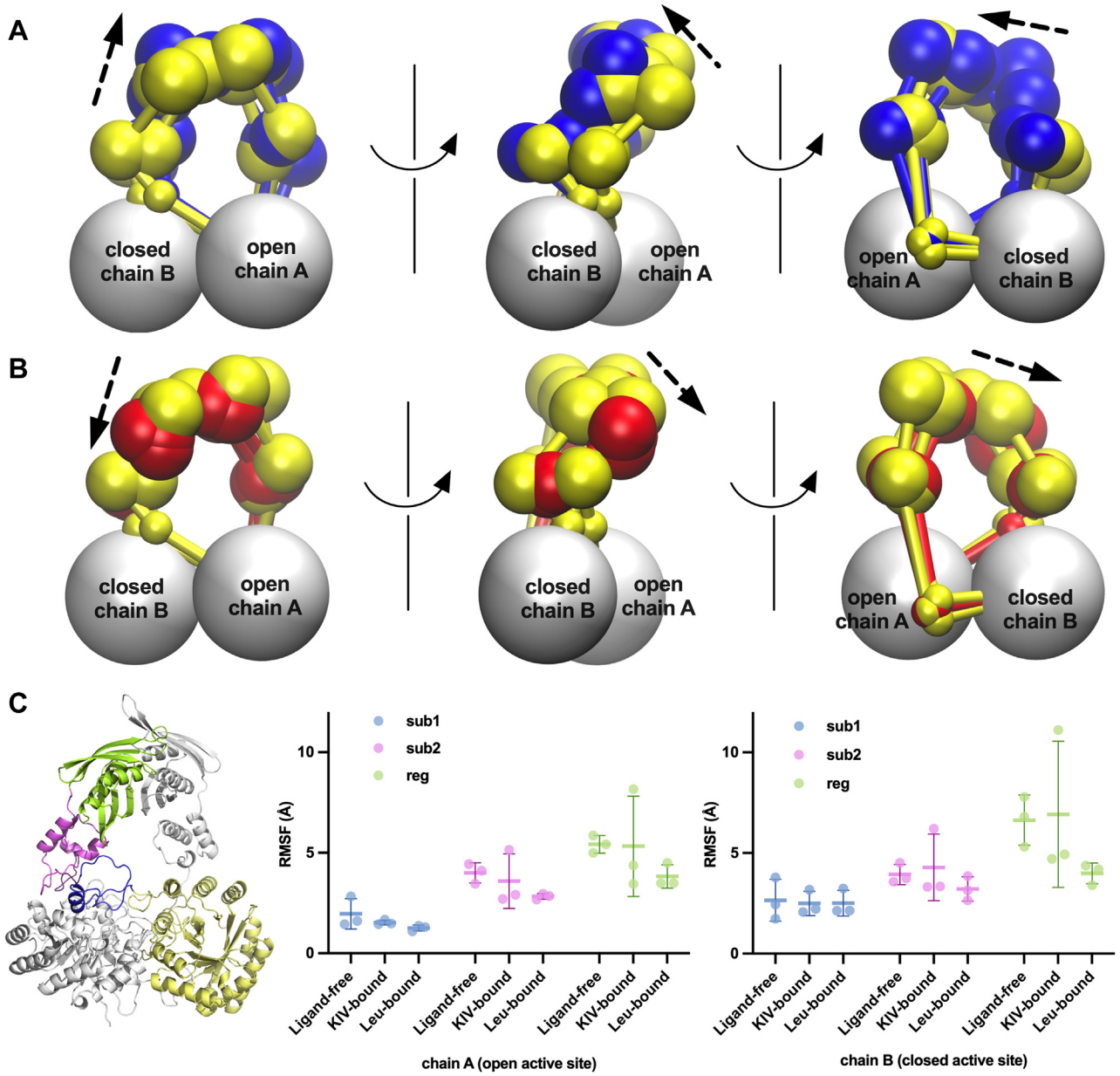

Figure 2. Changes in conformations and dynamics of the accessory domains of *Nme*IPMS associated with Leu binding revealed by MD simulations. Overall conformational changes in terms of subdomain positions (*A*) between ligand-free (*yellow*) and KIV-bound (*blue*) *Nme*IPMS and (*B*) between ligand-free (*yellow*) and Leu-bound (*red*) *Nme*IPMS. Each domain (catalytic barrel, subdomain 1 and linker, subdomain 2, and regulatory domain) is displayed as a *sphere* with its position defined by the mass-weighted center of mass of the corresponding domain, and the domains were joined by *cylinders*. The direction of movement from ligand-free to KIV-bound or Leu-bound conformations is indicated by *black dashed arrows*. *C*, fluctuations of the accessory domains were measured as RMSF values of the center of mass of the individual domains during each MD simulation. Individual RMSF values from the three replicate MD simulations are plotted, and the mean of the RMSF values is plotted as a *horizontal line*. The error bars are calculated as standard deviations. Trajectories were aligned at the N-terminal catalytic domains. KIV, ketoisovalerate; MD, molecular dynamics; *Nme*IPMS, IPMS from *Neisseria meningitides*; RMSF, root mean square fluctuation.

top of the active site of chain B in KIV-bound *Nme*IPMS, than that in ligand-free *Nme*IPMS, giving rise to a more open chain B active site in the KIV-bound system (Fig. 2*A*). Interestingly, comparison of MD average structures of Leu-bound and ligand-free *Nme*IPMS displayed the opposite trend (Fig. 2*B*). The active site of chain B in Leu-bound *Nme*IPMS was found in a more closed conformation than the ligand-free system, as the accessory and regulatory domains of chain A moved further in to cap the top of the active site of chain B.

The presence of Leu appeared to have also affected the domain dynamics in *Nme*IPMS (Fig. 2*B*). Positional fluctuations of the accessory and regulatory domains during MD simulations showed comparable levels of flexibilities between the ligand-free and KIV-bound *Nme*IPMS. However, Leu-bound *Nme*IPMS showed to some extent a reduction in fluctuations of subdomain II and the regulatory domain in both chains, indicating the Leu-bound conformations of *Nme*IPMS were more rigid.

In parallel, we examined the solution phase structures of *Nme*IPMS in the absence and presence of different ligands (α-KIV or Leu) using size-exclusion chromatography coupled with small-angle X-ray scattering (SEC–SAXS) experiments. SAXS data indicated that there were no significant changes in the average size and overall shape of *Nme*IPMS in the presence of either α-KIV or Leu, as demonstrated by the similar SAXS profiles and parameters obtained for ligand-free, KIV-bound, and Leu-bound *Nme*IPMS (Fig. 3*A* and Table 1). The SAXS data were compared with the theoretical scatterings of the average structures from MD simulations and showed reasonable consistencies between the observed and calculated structural profiles (Fig. S1). Ensemble fitting of the SAXS data using asymmetric MD average conformations and hypothetical symmetric conformations suggested that asymmetric conformations accounted for the majority of *Nme*IPMS structural populations in all the three experimental conditions (Fig. S2). The predicted SAXS scatterings from MD average structures of ligand-free, KIV-bound, and Leu-bound *Nme*IPMS were highly similar, which is consistent with the insignificant variations in the experimental scattering profiles. However, flexibility analysis using Porod–Debye transformations showed a structural rigidification of *Nme*IPMS in the presence of Leu (Fig. 3*B*) (28), matching the observed decreasing flexibilities of the accessory domains in MD simulations (Fig. 2*C*).

Leu binding is associated with changing polar interactions involving the accessory domains of Nme*IPMS*

The network of polar interactions established between different domains and chains of ligand-free, KIV-bound, and Leu-bound *Nme*IPMS during MD simulations was identified (Tables S2–S4), and the residues involved were mapped onto the corresponding MD average conformations (Fig. 4). In general, a larger number of polar interactions were established in the Leu-bound *Nme*IPMS that could stabilize its asymmetric conformations, in agreement with the reduced flexibility observed from both the MD simulations and SAXS experiments. A total of 16 polar interactions were established or became more stable in the inhibited Leu-bound *Nme*IPMS compared with the active KIV-bound *Nme*IPMS (Table 2). The position of chain A accessory domain over the closed chain B active site in the Leu-bound *Nme*IPMS was stabilized by clusters of polar interactions (*e.g.*, $Tyr313_A$–$Asp144_B$, $Ser299_A$–$Glu236_B$, $His297_A$–$Glu236_B$, and $Arg77_B$–$Asp304_A$). The relative position between accessory and regulatory domains of chain A in Leu-bound *Nme*IPMS was stabilized by the interaction between Arg310 and Glu503. On the other side of the dimer, the established polar interactions in the Leu-bound *Nme*IPMS formed a connected interaction pathway from the regulatory domain of chain B to the catalytic domain of chain A *via* chain B accessory domain, including $Arg470_B$–$Glu353_B$, $Arg476_B$–$Glu385_B$, $Tyr313_A$–$Asp144_B$, $Arg35_A$–$Asp345_B$, and $Arg32_A$–$Asp375_B$ (Fig. 4).

Generation of heterodimeric Nme*IPMS*

To identify the role of the accessory domains in the allosteric mechanism of *Nme*IPMS, we selected to probe two polar interactions ($Arg470_B$–$Glu353_B$ and $Arg32_A$–$Asp375_B$) in the pathway from the regulatory domain of chain B to the catalytic domain of chain A (Fig. 4). To account for the asymmetry of the interactions formed in the *Nme*IPMS homodimer, we first developed a protein assembly approach that enabled the

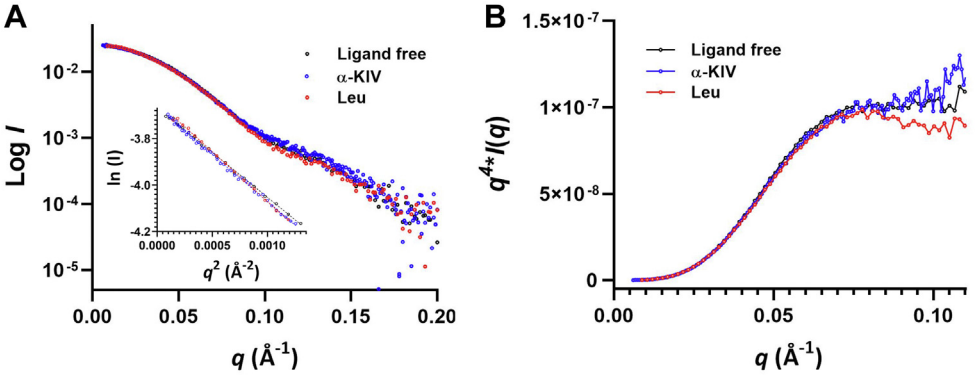

Figure 3. Analysis of the SAXS data for ligand-free *Nme*IPMS and *Nme*IPMS in the presence of α-KIV (*blue*) or Leu (*red*). *A*, SAXS profiles (log *I*(*q*) *versus q*) and their corresponding Guinier plots (ln *I*(*q*) *versus* q^2). *B*, Porod–Debye plot (q^4 * *I*(*q*) *versus q*) limited to the range of the SAXS data for which the Guinier linearity is observed. Each SAXS experiment in the presence of different ligands was repeated three times and presented consistent results. α-KIV, α-ketoisovalerate; Leu, leucine; *Nme*IPMS, IPMS from *Neisseria meningitides*; SAXS, small-angle X-ray scattering.

Table 1
SAXS parameters of ligand-free *Nme*IPMS and *Nme*IPMS in the presence of different ligand combinations

SAXS parameter	Ligands present		
	Ligand-free	α-KIV	Leu
Guinier analysis			
R_g (Å)	34.0 ± 0.4	34.7 ± 0.4	35.9 ± 0.5
I(0) (cm^{-1})	0.03 ± 0.00	0.03 ± 0.00	0.03 ± 0.00
Correlation coefficient, R^2	0.99	0.99	0.99
Pair wise distribution analysis			
R_g (Å)	34.1 ± 0.1	34.7 ± 0.3	35.8 ± 0.4
I(0) (cm^{-1})	0.03 ± 0.00	0.03 ± 0.00	0.03 ± 0.00
D_{max} (Å)	110.4	113.6	114.3
V_P (nm^3)	164	153	175
MM_{porod}			
MM (kDa)	96	90	103
Number of subunits	2	2	2

Abbreviation: MM_{porod}, molecular mass estimated from Porod volume.
The uncertainties represent standard deviations estimated by the error propagation from the experimental data.

generation of heterodimers of *Nme*IPMS to better pinpoint the effect of proposed substitutions on allosteric inhibition of *Nme*IPMS.

An expression vector pRSFDuet-1 that contained two independent expression cassettes was utilized, allowing simultaneous expressions of two polypeptide chains mediated by T7 RNA polymerase/promoter. Using restriction digestion and ligation reactions, two genes encoding *Nme*IPMS ORF that were N-terminally tagged with either a His tag or Strep tag were sequentially cloned into the pRSFDuet-1 vector and transformed into BL21 cells (Fig. 5). The monomeric units with different tags were expressed by IPTG induction and assembled as dimers either homogeneously or heterogeneously *in vivo*, forming His-tagged homodimer (*Nme*$IPMS_{His}$), Strep-tagged homodimer (*Nme*$IPMS_{Strep}$), and the heterodimer carrying both His and Strep tags (*Nme*$IPMS_{His/Strep}$) (Fig. 5). The dimeric species were separated by passing through two affinity columns, HisTrap and StrepTrap, which were specific to His tag and Strep tag (Fig. 5). Both *Nme*$IPMS_{His}$ and *Nme*$IPMS_{His/Strep}$ dimers were retained in the HisTrap, whereas *Nme*$IPMS_{strep}$ flowed through. The mixture eluted from the HisTrap was further separated by StrepTrap, which retained the heterodimer *Nme*$IPMS_{His/Strep}$. Mass spectrometry revealed the presence of both Strep- and His-tagged monomers. Both tags were then removed from the purified dimeric species by tobacco etch virus (TEV) protease cleavage and SEC.

Two polar interactions involving accessory subdomain II contribute to the communication of allosteric signals in Nme*IPMS*

The role of the polar interactions $Arg470_B$–$Glu353_B$ and $Arg32_A$–$Asp375_B$ in the allosteric mechanism of *Nme*IPMS were investigated by substituting Arg470 and Arg32 with Gln. Four variant enzymes were generated using the duet protein assembly method, including two heterodimers (*Nme*$IPMS_{R470Q}^{hetero}$ and *Nme*$IPMS_{R32Q}^{hetero}$) that contained the corresponding substitutions in only one chain and two homodimers (*Nme*$IPMS_{R470Q}$ and *Nme*$IPMS_{R32Q}$) that contained the substitutions in both chains. Kinetic properties of

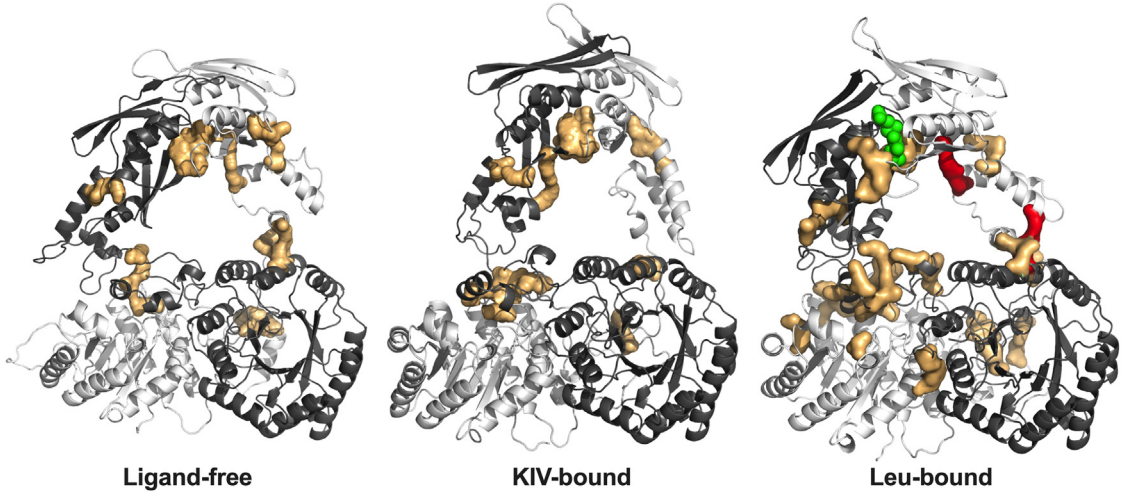

Figure 4. Polar interactions established with average occupancy above 30% during MD simulations for ligand-free, KIV-bound, and Leu-bound *Nme*IPMS. Residues involved in the interactions are displayed as *spheres* and surface representations in *light orange*. Leu molecules are displayed as *green spheres* in the Leu-bound structure. The two pairs of residues selected for amino acid substitution experiments are shown in *red*. KIV, ketoisovalerate; Leu, leucine; MD, molecular dynamics; *Nme*IPMS, IPMS from *Neisseria meningitides*.

Table 2
Hydrogen bonds and salt bridges with occupancy changes more than 30% between Leu-bound and KIV-bound *Nme*IPMS

H-bond donor	H-bond acceptor	Occupancy (KIV-bound) (%)	Occupancy (Leu-bound) (%)	Occupancy differences (%)	Domains
ARG362-Side (A)	GLU314-Side (A)	0	56	56	Subdomain II–subdomain I
TRP323-Side (A)	GLY291-Main (A)	0	42	42	Subdomain I–catalytic
ARG310-Side (A)	GLU503-Side (A)	0	41	41	Subdomain I–regulatory
ARG470-Side (B)	GLU353-Side (B)	0.19	78	78	Regulatory–subdomain II
ARG327-Side (B)	GLU298-Side (B)	38	84	45	Linker–subdomain I
ARG476-Side (B)	GLU385-Side (B)	0	44	44	Regulatory–subdomain II
ARG35-Side (A)	ASP345-Side (B)	0.72	59	59	Catalytic–subdomain II
THR461-Side (B)	ASP433-Side (A)	1.1	52	51	Regulatory–regulatory
ARG32-Side (A)	ASP375-Side (B)	0.93	46	45	Catalytic–subdomain II
LYS332-Side (A)	GLU18-Side (B)	0	43	43	Linker–catalytic
TYR313-Side (A)	ASP144-Side (B)	0	41	41	Subdomain I–catalytic
TYR180-Side (B)	ASP255-Side (A)	2.6	43	41	Catalytic–catalytic
SER299-Side (A)	GLU236-Side (B)	37	73	36	Subdomain I–catalytic
HSD297-Side (A)	GLU236-Side (B)	20	55	34	Subdomain I–catalytic
LYS332-Side (A)	ASP56-Side (B)	9.2	42	33	Linker–catalytic
ARG77-Side (B)	ASP304-Side (A)	5.5	37	31	Catalytic–subdomain I
ARG476-Side (A)	GLU385-Side (A)	37	0	−37	Regulatory–subdomain II
LYS501-Side (B)	GLU385-Side (B)	50	13	−37	Regulatory–subdomain II

Positive occupancy differences indicate the interactions were formed in Leu-bound *Nme*IPMS, and negative differences indicate the interactions were broken in Leu-bound *Nme*IPMS.

the variant enzymes and their inhibition responses to Leu were characterized and compared with the WT enzyme.

The kinetic assays showed that R32Q and R470Q substitutions had a small effect on the catalytic activity of *Nme*IPMS, except in *Nme*IPMS$_{R32Q}$, where the turnover number (k_{cat}) was decreased by half (Table 3).

In contrast, R470Q and R32Q substitutions had striking impacts on the allosteric inhibition responses to Leu in the homodimeric variants (*Nme*IPMS$_{R470Q}$ and *Nme*IPMS$_{R32Q}$). The apparent inhibitory constants (K_i) of Leu with respect to either AcCoA or α-KIV showed significant increases in *Nme*IPMS$_{R470Q}$ and *Nme*IPMS$_{R32Q}$ compared with the WT enzyme (Table 3). Interestingly, the heterodimeric variants *Nme*IPMS$_{R470Q}^{hetero}$ and *Nme*IPMS$_{R32Q}^{hetero}$ showed only small increases in K_i values (Table 3), suggesting that maintaining the connected polar interaction pathway on one side of the dimer was sufficient to stabilize the Leu-bound conformation and achieve allosteric inhibition. This observation supported the predicted asymmetry of the polar interaction networks exposed by MD simulations.

The effect of the R32Q or R470Q substitutions on Leu binding was inspected using the NMR technique water-ligand observed *via* gradient spectroscopy (waterLOGSY) (Fig. S3) (29). Disassociation constants (K_D) calculated from the waterLOGSY data demonstrated that all the four variants maintained similar affinities for Leu to that in the WT

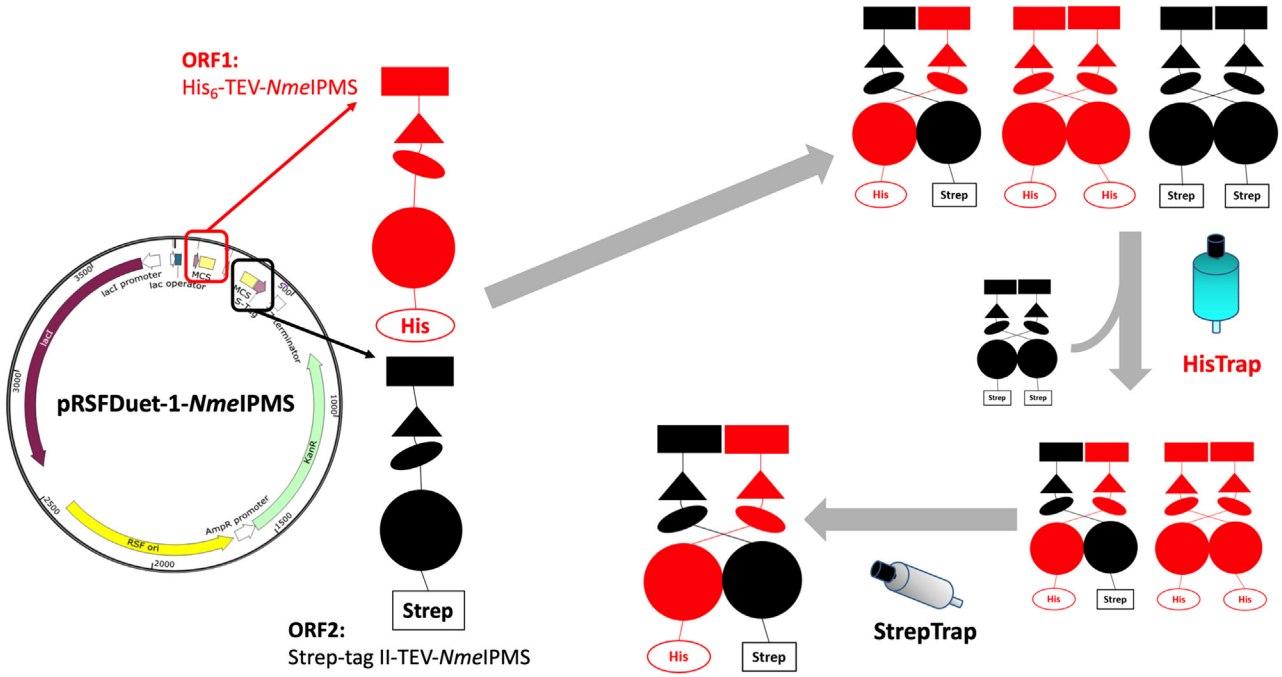

Figure 5. Schematic illustration of the homodimeric and heterodimeric assemblies of His-tagged and Strep-tagged *Nme*IPMS and a two-step purification method using HisTrap and StrepTrap in sequence for separating three dimeric species of *Nme*IPMS. *NmeIPMS*, IPMS from *Neisseria meningitides*.

Table 3
Kinetic characterizations of WT and variant *Nme*IPMS enzymes and Leu inhibition effect on WT and variant *Nme*IPMS enzymes

SAXS parameter	K_m^{AcCoA} (μM)	K_m^{KIV} (μM)	k_{cat} (s^{-1})	k_{cat}/K_m^{AcCoA} ($\mu M^{-1}.\ s^{-1}$)	k_{cat}/K_m^{KIV} ($\mu M^{-1}.\ s^{-1}$)	$K_i^{App,AcCoA}$ (μM)	$K_i^{App,KIV}$ (μM)
*Nme*IPMS	39 ± 5	37 ± 5	12.8 ± 0.3	0.33	0.35	43 ± 4	48 ± 3
*Nme*IPMS$_{R32Q}^{hetero}$	35 ± 5	48 ± 6	12 ± 0.5	0.34	0.25	70 ± 4	84 ± 6
*Nme*IPMS$_{R32Q}$	40 ± 5	47 ± 3	5.4 ± 0.2	0.14	0.11	7624 ± 2223	10,913 ± 4453
*Nme*IPMS$_{R470Q}^{hetero}$	38 ± 4	37 ± 3	15.4 ± 0.3	0.41	0.42	61 ± 3	70 ± 4
*Nme*IPMS$_{R470Q}$	48 ± 3	53 ± 6	14.2 ± 0.6	0.30	0.27	5291 ± 1067	4147 ± 1399

To determine apparent K_i values, three Leu concentrations (20, 50, and 100 μM) were applied separately in the kinetic assays where either AcCoA or α-KIV was fixed at 300 μM.

*Nme*IPMS (Table 4 and Fig. S4), suggesting that the loss of allosteric inhibition in the homodimeric variants *Nme*IPMS$_{R470Q}$ and *Nme*IPMS$_{R32Q}$ was not because of loss of the allosteric binding but was the result of disrupted allosteric signal.

Discussion

The gateway enzyme of the Leu biosynthesis pathway, IPMS, is a dynamic multidomain enzyme with the constituent domains joined by flexible linkers. IPMS adopts a domain-swapped homodimer quaternary structure with asymmetry illustrated by the markedly different relative domain conformations of the two chains in the crystal structures of *Mtu*IPMS (23). Owing to challenges posed to structural studies because of the dynamic and asymmetric nature of IPMS enzymes, the roles of structural dynamics and asymmetry in the allosteric mechanisms are yet to be fully understood.

Previous hydrogen/deuterium exchange experiments on *Mtu*IPMS revealed a shift in conformational equilibria of subdomain II in the presence of the allosteric inhibitor Leu (27). Here, we investigated the allosteric mechanism of *Nme*IPMS using MD simulations and SAXS experiments. We found that, similar to what was observed for *Mtu*IPMS, allosteric inhibition of *Nme*IPMS was associated with positional changes and reduced flexibilities of the accessory domains.

MD simulations revealed a network of asymmetric interdomain polar interactions differentially stabilizing the Leu-bound conformation of *Nme*IPMS. We chose to probe the contributions of two interactions, $Arg470_B$–$Glu353_B$ and $Arg32_A$–$Asp375_B$, by substituting Arg470 or Arg32 with Gln. Using a dual expression protein assembly approach, we generated two homodimeric (*Nme*IPMS$_{R470Q}$ and *Nme*IPMS$_{R32Q}$) and two heterodimeric (*Nme*IPMS$_{R470Q}^{hetero}$ and *Nme*IPMS$_{R32Q}^{hetero}$) variants. We observed that the complete loss of these interdomain interactions was detrimental to the communication of the allosteric signal in the homodimeric variants, as the allosteric response was significantly impaired despite Leu binding not being compromised.

Table 4
K_D constants showing the affinities of *Nme*IPMS and its variants for Leu obtained from waterLOGSY assays

*Nme*IPMS	K_D (μM)
*Nme*IPMS	376 ± 48
*Nme*IPMS$_{R32Q}^{hetero}$	352 ± 37
*Nme*IPMS$_{R32Q}$	324 ± 65
*Nme*IPMS$_{R470Q}^{hetero}$	386 ± 72
*Nme*IPMS$_{R470Q}$	370 ± 55

Previous studies also identified Tyr410 in *Mtu*IPMS to be essential for allostery (25, 27). Here, the equivalent residue in *Nme*IPMS, Tyr313, was also found to establish asymmetric interdomain polar interactions in the presence of Leu (Table 2). In general, it appears that the conformational dynamic changes in the accessory domains associated with allostery in *Nme*IPMS were stabilized by these interdomain polar interactions, and allosteric inhibition was achieved by locking *Nme*IPMS in the rigid Leu-bound conformational state.

In contrast to the homodimeric variants, which completely lost the ability to establish the interdomain interactions, the heterodimeric variants retained the ability to form the interdomain interactions on one side of the dimer. Interestingly, we observed that the allosteric response to Leu was maintained in these heterodimeric variants, with only small increases in K_i values. These observations suggested that establishing the interdomain polar interactions on one side of the dimer was sufficient to lock the enzyme in the inhibited rigid conformations and underscored the importance of asymmetry in the allosteric mechanism of *Nme*IPMS.

IPMS is closely related to the enzyme citramalate synthase (CMS) (30), which is the first enzyme in the threonine-independent pathway of isoleucine biosynthesis and is feedback inhibited by the pathway end product Ile (31). Crystal structures of separate catalytic and regulatory domains of CMS exhibit high structural similarities to those of *Mtu*IPMS (31, 32); however, the full structure of CMS is yet to be obtained. Based on sequence similarity, CMS likely adopts similar domain organizations and asymmetric conformations as IPMS, with the dynamic accessory domain between the catalytic TIM barrel and the regulatory domain that binds Ile. Therefore, we predict that CMS may also adopt a very similar allosteric mechanism to IPMS. Another closely related enzyme to IPMS is homocitrate synthase (HCS), which catalyzes the first step in lysine biosynthesis (33, 34). HCS is dimeric and consists of only catalytic TIM barrel domains and flexible accessory domains but lacks the regulatory domains. HCS is feedback regulated by the pathway end product lysine by competitive inhibition at the active site (33, 35–37). Interestingly, the dimeric structures of HCS appear to be symmetric, which suggests that appending regulatory domain dimers to the accessory domains likely leads to the asymmetry that is integral to the allosteric mechanisms in IPMS and CMS.

In summary, here we showed that the interdomain flexibility between the accessory and the catalytic domains is key to IPMS catalysis. We probed interactions that communicate allosteric signal to the active site of IPMS using mutagenesis

Table 5
Primers for construction of expression vectors

Duet_I_FW1	TGTATTTTCAGGGCATGACACAGACCAAC
Duet_I_FW2	AAAGGATCCGGAAAACCTGTATTTTCAGG
Duet_I_RV	AACAAGCTTTCATCAAATCGTACCGCTGC
Duet_II_FW1	CGAAAAAGAAAACCTGTATTTTCAGGGCATGACACAGACCAACC
Duet_II_FW2	AAAAGATCTCTGGAGCCACCCGCAGTTCGAAAAAGAAAACCTG
Duet_II_RV	AAAACTCGAGTCATCAAATCGTACCGCTGCCCTGCGC
Duet_R32Q_FW	AAGAGGAAAAAATCCAGGTCGCCCGCCAGCTGG
Duet_R32Q_RV	CCAGCTGGCGGGCGACCTGGATTTTTTCCTCTT
Duet_R470Q_FW	AAACCAGCGTCCAACTGGCGCGCGGC
Duet_R470Q_RV	GCCGCGCGCCAGTTGGACGCTGGTTT

Abbreviations: *GGATCC, BamH I* restriction site; *AAGCTT, Hind III* restriction site; *AGATCT, Bgl II* restriction site; *CTCGAG, Xho* I restriction site.
The designated mutations are highlighted in red.

and demonstrated that the contacts formed in the asymmetric conformation are manifestly important for allostery. Allostery in IPMS exploits the vulnerability of the enzyme to asymmetric conformations, and inhibition is achieved by putting constraints on the accessible conformations *via* stabilizing interdomain interactions.

Experimental procedures

Construction of plasmids

The expression plasmid carrying the gene encoding *Nme*IPMS with a cleavable N-terminal His tag, pFH01, was already available from previous work (22). To construct duet *Nme*IPMS expression plasmid, a two-step gene cloning was conducted using pFH01 as PCR template to insert *Nme*IPMS gene into multiple cloning sites (MCSs) 1 and 2 of pRSFDuet1 (Merck) sequentially. In the first step, *Nme*IPMS gene was amplified *via* two rounds of PCR using two pairs of primers, Duet_I_FW1/Duet_I_RV and Duet_I_FW2/Duet_I_RV (Table 5), in sequence to introduce an N-terminal TEV protease cleavage site (*in bold*) and BamHI and HindIII restriction sites (*underlined*). After gel purification, the final PCR product was doubly digested by BamHI and HindIII and then ligated into the MSC 1 and transformed into *Escherichia coli* DH5α-competent cells. The recombinant pRSFDuet1-MSC1-*Nme*IPMS plasmid was isolated from the transformant screened by LB agar medium containing 100 μg/ml kanamycin and verified by gene sequencing. It is worth noting that pRSFDuet1 contains a gene sequence encoding 6× His at the upstream of MSC 1, thus His-tag sequence was not included in the Duet_I_FW2 primer. In the second step, *Nme*IPMS gene was amplified and incorporated with a sequence encoding an N-terminal Strep tag (*in italic*), a TEV cleavage site (*in bold*) between the Strep tag and *Nme*IPMS gene, and restriction sites, BglII and XhoI (*underlined*). To achieve this, two rounds of PCR were carried out sequentially using two primer pairs, Duet_II_FW1/Duet_II_RV and Duet_II_FW2/Duet_II_RV (Table 5). Following gel purification, BglII/XhoI digestion, ligation and transformation as described in step 1, the PCR product was inserted into MCS 2 of pRSFDuet1-MSC1-*Nme*IPMS. The obtained recombinant construct (pRSFDuet1-*Nme*IPMS) carries two *Nme*IPMS ORFs, respectively, at two MCS sites. As well, the ORFs at MCS 2 of pRSFDuet1-*Nme*IPMS were sequence verified.

Single mutations, R32Q or R470Q, were introduced into the His-tagged *Nme*IPMS ORF at MSC 1 of pRSFDuet1-*Nme*IPMS using overlap extension-PCR–based site-directed mutagenesis and a pair of mutagenic primers containing the designated mutation (*in red*). Three rounds of PCR were included in the mutagenesis procedure, two of which were carried out using pFH01 as the template, and respectively, using two primer pairs, Duet_I_FW2/reverse mutagenic primer (Duet_R32Q_RV for R32Q and Duet_R470Q_RV for R470Q) and forward mutagenic primer (Duet_R32Q_FW for R32Q and Duet_R470Q_FW for R470Q)/Duet_I_RV. The resulting two PCR products having an overlapping segment were purified and mixed as the template for the final PCR using primers, Duet_I_FW2/Duet_I_RV. This PCR generated a full-length gene sequence encoding *Nme*IPMS with the designated mutation, which is then purified and cloned into the MCS 1 of pRSFDuet1-*Nme*IPMS to substitute for the WT *Nme*IPMS ORF. The plasmid carrying the mutation variant R32Q or R470Q at MCS 1 (pRSFDuet1-R32Q/WT or pRSFDuet1-R470Q/WT) was sequence verified.

Protein expression and purification

Plasmids pFH01, pRSFDuet1-*Nme*IPMS, pRSFDuet1-R32Q/WT, and pRSFDuet1-R470Q/WT were transformed into *E. coli* BL21 (DE3) competent cells for protein expression. Cultures were grown at 37 °C in LB medium supplemented with 100 μg/ml ampicillin for the cell strain containing pFH01 or 100 μg/ml kanamycin for the cells transformed by duet-expression plasmids. Expression of target protein was induced by the addition of 0.5 mM IPTG into the culture at midexponential phase, which is followed by further overnight growth at 23 °C.

Cells were harvested by centrifugation (12,000*g* for 15 min at 4 °C) and resuspended in lysis buffer (20 mM sodium phosphate buffer [pH 8.0], 500 mM NaCl, 20 mM imidazole, and 2 mM DTT). Cells were lysed by sonication and clarified by centrifugation (40,000*g* for 40 min at 4 °C).

Standard purification of Nme*IPMS*

The clarified cell lysate containing WT His-tagged *Nme*IPMS encoded by pFH01 was filtered and loaded to a HisTrap HP column (GE Healthcare), pre-equilibrated with binding buffer (20 mM sodium phosphate buffer [pH 8.0], 500 mM NaCl, and 20 mM imidazole), and then eluted with elution buffer (20 mM sodium phosphate buffer [pH 8.0], 500 mM NaCl, and 500 mM imidazole). The eluted fractions were pooled together and desalted, which was followed by

overnight treatment of TEV protease at 4 °C to cleave the His tag. After TEV cleavage, the protein was reapplied to the HisTrap column to remove the TEV protease, the His tag, and any noncleaved protein. The untagged proteins were further purified by SEC (HiPrep 16/60 Sephacryl S-200 HR column; GE Healthcare) using a buffer consisting of 20 mM Bis–Tris propane buffer (pH 8.5), 200 mM NaCl, and 10 mM $MgCl_2$.

Separation of dimeric species expressed by duet expression plasmids

The crude cell extract containing the expression products of pRSFDuet1-*Nme*IPMS or pRSFDuet1-R32Q/WT or pRSFDuet1-R470Q/WT was subjected to a HisTrap to retain the His-tagged dimeric species following the standard procedure as described previously. The elution fraction from HisTrap was transferred to Strep-Tactin binding buffer (20 mM sodium phosphate buffer [pH 7.4], 280 mM NaCl, and 6 mM KCl) and subsequently loaded to a StrepTrap column HP (GE Healthcare) pre-equilibrated with Strep-Tactin binding buffer. The homodimeric His-tagged *Nme*IPMS or variants flew through StrepTrap column, whereas the heterodimeric species carrying a His tag and a Strep tag was retained in the column, which was then eluted by the Strep-Tactin binding buffer supplemented with 2.5 mM desthiobiotin. The separated homodimeric and heterodimeric species were individually treated by TEV protease and subjected to SEC in sequence following the standard purification procedure for removal of tags and further purification.

Kinetic assay

The rate of *Nme*IPMS catalyzed reaction was measured by a dithiodipyridine (DTP)-coupled assay, which uses DTP to monitor the formation of CoA product at 324 nm (ε = 1.98×10^4 l × M^{-1} cm^{-1}). All kinetic assays were carried out in 1 cm path length quartz cuvettes at 25 °C and measured by a Varian Cary 100 UV–visible spectrophotometer. The typical reaction condition contained 100 μM DTP, 20 mM KCl, 20 mM $MgCl_2$, and 3.0×10^{-2} μM enzyme in 50 mM HEPES buffer (pH 7.5), and all reactions were initiated by the addition of α-KIV. To determine apparent kinetic parameters of WT *Nme*IPMS and variant enzymes, the α-KIV concentration was fixed at 300 μM, and the concentration of AcCoA was fixed at 300 μM, while carrying out assays with varied concentrations of the other substrates.

Leu inhibition assay

The inhibitory effect of Leu on activities of WT *Nme*IPMS and variant enzymes was characterized under the standard kinetic reaction condition. To determine the apparent K_i value for Leu with respect to either substrate, kinetic assays were conducted at three Leu concentrations (20, 50, and 100 μM) separately where the α-KIV concentration was fixed at 300 μM or the AcCoA concentration was fixed at 300 μM, whereas varied the concentration of the other substrate. The recorded data with respect to either α-KIV or AcCoA were analyzed by Prism and fits to noncompetitive inhibition model well.

SAXS

SAXS measurements were conducted at the Australian Synchrotron SAXS/WAXS beamline equipped with a Pilatus detector (1 M, 170 × 170 mm, effective pixel size, 172 × 172 mm) (38–40). The applied wavelength of X-ray was 1.0332 Å, and a sample detector at a distance of 1.6 m from the sample, which recorded scattered X-ray intensities covering the q range of 0.0015 to 3.0 $Å^{-1}$. The q is the magnitude of the scattering vector, which is defined as $q = (4\pi/\lambda)\sin\theta$, where λ is the wavelength and 2θ is scattering angle. The WT *Nme*IPMS was eluted from a SEC column (Superdex increase 200 5/150; GE Healthcare) using the ligand-free SEC–SAXS buffer (20 mM Bis–Tris propane buffer [pH 8.5], 200 mM NaCl, 10 mM $MgCl_2$, and 3% [v/v] glycerol) or the buffers, respectively, containing 500 μM α-KIV and Leu. The elution traces in all applied conditions showed nicely consistent single peaks (Fig. S5). The eluted sample passed into a 1.0 mm thin-walled glass capillary where the sample was detected using X-rays at 25 °C at 1 s intervals. The reduction and buffer subtraction of raw scattering data was performed by Scatterbrain developed at the Australian Synchrotron. Processed data were plotted as $I(q)$ *versus* q and analyzed using Primus (Biological Small Angle Scattering Group) (41). Each SAXS dataset containing ∼650 data frames over the range $0.005 \le q \le 0.35$ $Å^{-1}$ where a single symmetric scattering peak over ∼80 frames was observed. To verify conformational homogeneity, three groups of frames, respectively, covering the maximum scattering intensity and either side of the scattering maximum were summed and compared. The same scattering profile was observed across each scattering peak. Guinier plots ($\ln I(q)$ *versus* q^2) of scattering data showing good linearity in the q range of $q \ge 1.3/R_g$ demonstrated good monodispersity of samples and evaluated the R_g of the protein particle. The Porod volume (V_p) and the maximum distance (D_{max}) of the protein particle were evaluated, respectively, from the Porod plot and the pair-distance distribution ($P(r)$) function obtained *via* Fourier transformation. MM_{porod} (molecular mass estimated from Porod volume) was obtained by dividing the Porod volumes by 1.7.

WaterLOGSY

WaterLOGSY can be used to detect ligand–protein binding *via* ^{1}H NMR observation of small-molecule ligand (29, 42). In solution, proton (^{1}H) magnetization of small-molecule ligand can be transferred directly from excited bulk water molecules or indirectly from excited proton at protein surface through protein–ligand complex. Direct and indirect magnetization transferring, respectively, yields positive and negative nOe signals, which is taken advantageous of by waterLOGSY to quantify the ligand bound to protein for further analysis of protein–ligand affinity.

WaterLOGSY spectra were recorded at a ^{1}H frequency of 600 MHz using a JEOL 600 MHz Nuclear Magnetic Resonance Spectrometer type JNM-ECZ600R with a 5 mm FG/RO Digital Auto Tune Probe, at 25 °C. A 5 mm diameter NMR tube with a sample volume of 600 μl was used in all experiments.

Samples consisted of 10 mM Hepes (pH 8.0), 3 mM $MgCl_2$, 3 mM KCl, 10% (v/v) D_2O, and Leu at varied concentrations (0, 50, 150, 250, 500, and 750 μM). WaterLOGSY experiments were conducted using the pulse sequence without a water flipback pulse as described by Dalvit *et al.* (29). The parameter used was a 30 ms pulse length with an initial water selective 180° REBURP pulse. W5 composite inversion pulses were used for a double-pulsed field gradient spin echo WATERGATE water signal suppression. The mixing time was 1 s and a 2 s relaxation delay before each scan was used. A T1p Filter was used to suppress the protein signals.

WaterLOGSY spectrum for each sample was recorded in the absence of enzyme first, which was followed by a second measurement with the addition of enzyme (WT *Nme*IPMS, or *Nme*$IPMS_{R32Q}$ or *Nme*$IPMS_{R32Q}^{hetero}$, or *Nme*$IPMS_{R470Q}$ or *Nme*$IPMS_{R470Q}^{hetero}$) with a final concentration of 10 μM. Subtraction of the two waterLOGSY signal intensities recorded, respectively, in the absence and presence of enzyme at varied Leu concentration resulted in the Leu-binding isotherm. K_D value was obtained by fitting the binding isotherm to the equation as follows (43–45):

$$I = \frac{I_{max} + [L_T]}{K_D \times [L_T]}$$

where I denoted changes in corrected waterLOGSY intensity resulted by titrations. I_{max} indicates the maximum intensity change. $[L_T]$ is the concentration of titrated ligand.

Homology model and MD simulations

The full structural model of KIV-bound *Nme*IPMS was first generated by homology modeling using Prime (Schrödinger) (46, 47). The crystal structure of KIV-bound *Mtu*IPMS (PDB ID: 1SR9) was used as the template, which shares 31% homology to the amino acid sequence of *Nme*IPMS. The metal ion in the active site of *Nme*IPMS was modeled as Mg^{2+} (whereas in *Mtu*IPMS crystal structure, Zn^{2+} ions were bound). The α-KIVs in the active site of *Mtu*IPMS were kept in the homology model, and metal coordination to α-KIVs observed in *Mtu*IPMS was retained. Ligand-free *Nme*IPMS model was then obtained by deleting the α-KIVs in the active sites but keeping the Mg^{2+} ion. Leu-bound *Nme*IPMS was generated by merging the Leu molecules bound in the regulatory domain of *Mtu*IPMS (PDB ID: 3FIG) onto corresponding Leu-binding sites in the ligand-free *Nme*IPMS homology model. The homology models adopted the same asymmetric conformation as in the crystal structure of *Mtu*IPMS and align to the crystal structure of *Mtu*IPMS (PDB ID: 1SR9) with an RMSD value of 1.2 Å (aligning backbone atoms). The catalytic domains in the homology models compared well to the crystal structure of the isolated catalytic domains of *Nme*IPMS (PDB ID: 3RMJ), with an RMSD value of 2.2 Å (aligning backbone atoms of residues 1–297).

MD simulations were conducted using NAMD 2.12 (Theoretical and Computational Biophysics Group at the University of Illinois), and trajectories were visualized and analyzed in VMD. The *Nme*IPMS systems were solvated in a water box with explicit TIP3P water molecules, and the charges were neutralized by adding Na^+ and Cl^- ions. Initial force field topology and parameters for α-KIV were obtained from CGenFF server (https://cgenff.paramchem.org) (48–51) and further refined by Force Field Toolkit (52). MD simulations were conducted with CHARMM36 force field (53) at a constant temperature of 310 K and pressure of 1 atm. For MD simulations of ligand-free and KIV-bound *Nme*IPMS, the systems were first minimized for 5000 steps followed by dynamic production runs at 2 fs time steps. For Leu-bound *Nme*IPMS, the simulation system was first relaxed with two phases of short MD simulations. The first phase consisted of a series of 20 simulations, each started with 5000 steps of minimization followed by 0.1 ns of dynamics simulation. The second phase of relaxation consisted of 80 simulations, each started with 5000 steps of minimization followed by 1 ns of dynamics simulation. The production run for Leu-bound *Nme*IPMS was started after the relaxation runs. Three replicates of MD simulations were conducted for ligand-free (310.9, 357.4, and 239.9 ns), KIV-bound (360.7, 298.8, and 239.1 ns), and Leu-bound (332.4, 282.3, and 191.4 ns for production runs) *Nme*IPMS. The RMSD values of protein backbone atoms during the MD simulations were plotted, and the equilibrated periods were identified for analyses (Fig. S6). A total of 648.2, 563.6, and 606.1 ns of equilibrated trajectories were obtained for ligand-free, KIV-bound, and Leu-bound *Nme*IPMS systems, respectively. It should be noted that the lattice contacts in the crystal structure of *Mtu*IPMS that may have stabilized the packing of the asymmetric conformation were neither in the *Nme*IPMS homology models nor in the MD simulations; therefore, the observed asymmetric conformations from MD simulations were not likely to be biased by those lattice contacts.

Data availability

The data for the experimental work described herein are available on request by email to emily.parker@vuw.ac.nz.

Supporting information—This article contains supporting information.

Acknowledgments—We acknowledge the contribution of NeSI high-performance computing facilities to the results of this research. NZ's national facilities are provided by the NZ eScience Infrastructure and funded jointly by NeSI's collaborator institutions and through the Ministry of Business, Innovation & Employment's Research Infrastructure programme. URL: https://www.nesi.org.nz. Data were collected at the SAXS beamlines of the Australian Synchrotron with access provided by the New Zealand Synchrotron Group. Funding for this work was provided by the New Zealand Marsden Fund (grant no.: VUW1426).

Author contributions—Y. B., W. J., and E. J. P. conceptualization; Y. B., W. J., and J. V. methodology; Y. B. and W. J. investigation; Y. B. and W. J. writing–original draft; W. J. and E. J. P. writing–review & editing; E. J. P. supervision; E. J. P. project administration; E. J. P. funding acquisition.

Conflict of interest—The authors declare that they have no conflicts of interest with the contents of this article.

Abbreviations—The abbreviations used are: α-KIV, α-ketoisovalerate; AcCoA, acetyl-coenzyme A; CMS, citramalate synthase; DTP, dithiodipyridine; HCS, homocitrate synthase; IPMS, α-isopropylmalate synthase; *Lbi*IPMS, IPMS from *Leptospira biflexa*; Leu, leucine; MCS, multiple cloning site; MD, molecular dynamics; *Mtu*IPMS, IPMS from *Mycobacterium tuberculosis*; *Nme*IPMS, IPMS from *Neisseria meningitides*; PDB, Protein Data Bank; SEC–SAXS, size-exclusion chromatography coupled with small-angle X-ray scattering; TEV, tobacco etch virus.

References

1. Kerns, S. J., Agafonov, R. V., Cho, Y. J., Pontiggia, F., Otten, R., Pachov, D. V., *et al.* (2015) The energy landscape of adenylate kinase during catalysis. *Nat. Struct. Mol. Biol.* **22**, 124–131
2. Ma, B., and Nussinov, R. (2016) Protein dynamics: conformational footprints. *Nat. Chem. Biol.* **12**, 890–891
3. Nussinov, R., and Wolynes, P. G. (2014) A second molecular biology revolution? The energy landscapes of biomolecular function. *Phys. Chem. Chem. Phys.* **16**, 6321–6322
4. Wei, G., Xi, W., Nussinov, R., and Ma, B. (2016) Protein ensembles: how does nature harness thermodynamic fluctuations for life? The diverse functional roles of conformational ensembles in the cell. *Chem. Rev.* **116**, 6516–6551
5. Popovych, N., Sun, S., Ebright, R. H., and Kalodimos, C. G. (2006) Dynamically driven protein allostery. *Nat. Struct. Mol. Biol.* **13**, 831–838
6. Goodey, N. M., and Benkovic, S. J. (2008) Allosteric regulation and catalysis emerge via a common route. *Nat. Chem. Biol.* **4**, 474–482
7. Jiao, W., Hutton, R. D., Cross, P. J., Jameson, G. B., and Parker, E. J. (2012) Dynamic cross-talk among remote binding sites: the molecular basis for unusual synergistic allostery. *J. Mol. Biol.* **415**, 716–726
8. Liu, J., and Nussinov, R. (2016) Allostery: an overview of its history, concepts, methods, and applications. *PLoS Comput. Biol.* **12**, e1004966
9. Jiao, W., Mittelstädt, G., Moggré, G. J., and Parker, E. J. (2019) Hinge twists and population shifts deliver regulated catalysis for ATP-PRT in histidine biosynthesis. *Biophys. J.* **116**, 1887–1897
10. Maria-Solano, M. A., Iglesias-Fernández, J., and Osuna, S. (2019) Deciphering the allosterically driven conformational ensemble in tryptophan synthase evolution. *J. Am. Chem. Soc.* **141**, 13049–13056
11. Light, S. H., and Anderson, W. F. (2013) The diversity of allosteric controls at the gateway to aromatic amino acid biosynthesis. *Protein Sci.* **22**, 395–404
12. Gerhart, J. (2014) From feedback inhibition to allostery: the enduring example of aspartate transcarbamoylase. *FEBS J.* **281**, 612–620
13. Soares da Costa, T. P., Abbott, B. M., Gendall, A. R., Panjikar, S., and Perugini, M. A. (2018) Molecular evolution of an oligomeric biocatalyst functioning in lysine biosynthesis. *Biophys. Rev.* **10**, 153–162
14. Semmelmann, F., Straub, K., Nazet, J., Rajendran, C., Merkl, R., and Sterner, R. (2019) Mapping the allosteric communication network of aminodeoxychorismate synthase. *J. Mol. Biol.* **431**, 2718–2728
15. Jiao, W., Lang, E. J., Bai, Y., Fan, Y., and Parker, E. J. (2020) Diverse allosteric componentry and mechanisms control entry into aromatic metabolite biosynthesis. *Curr. Opin. Struct. Biol.* **65**, 159–167
16. Huisman, F. H., Koon, N., Bulloch, E. M., Baker, H. M., Baker, E. N., Squire, C. J., *et al.* (2012) Removal of the C-terminal regulatory domain of α-isopropylmalate synthase disrupts functional substrate binding. *Biochemistry* **51**, 2289–2297
17. Lang, E. J., Cross, P. J., Mittelstädt, G., Jameson, G. B., and Parker, E. J. (2014) Allosteric ACTion: the varied ACT domains regulating enzymes of amino-acid metabolism. *Curr. Opin. Struct. Biol.* **29**, 102–111
18. Mittelstädt, G., Jiao, W., Livingstone, E. K., Moggré, G. J., Nazmi, A. R., and Parker, E. J. (2018) A dimeric catalytic core relates the short and long forms of ATP-phosphoribosyltransferase. *Biochem. J.* **475**, 247–260
19. Bai, Y., and Parker, E. J. (2021) Reciprocal allostery arising from a bienzyme assembly controls aromatic amino acid biosynthesis in *Prevotella nigrescens*. *J. Biol. Chem.* **297**, 101038
20. de Carvalho, L. P., Argyrou, A., and Blanchard, J. S. (2005) Slow-onset feedback inhibition: inhibition of *Mycobacterium tuberculosis* α-isopropylmalate synthase by L-leucine. *J. Am. Chem. Soc.* **127**, 10004–10005
21. Leary, T. R., and Kohlhaw, G. B. (1972) α-isopropylmalate synthase from *Salmonella typhimurium*. Analysis of the guaternary structure and its relation to function. *J. Biol. Chem.* **247**, 1089–1095
22. Huisman, F. H., Hunter, M. F., Devenish, S. R., Gerrard, J. A., and Parker, E. J. (2010) The C-terminal regulatory domain is required for catalysis by *Neisseria meningitidis* α-isopropylmalate synthase. *Biochem. Biophys. Res. Commun.* **393**, 168–173
23. Koon, N., Squire, C. J., and Baker, E. N. (2004) Crystal structure of LeuA from *Mycobacterium tuberculosis*, a key enzyme in leucine biosynthesis. *Proc. Natl. Acad. Sci. U. S. A.* **101**, 8295–8300
24. Zhang, Z., Wu, J., Lin, W., Wang, J., Yan, H., Zhao, W., *et al.* (2014) Subdomain II of α-isopropylmalate synthase is essential for activity: inferring a mechanism of feedback inhibition. *J. Biol. Chem.* **289**, 27966–27978
25. de Carvalho, L. P., Frantom, P. A., Argyrou, A., and Blanchard, J. S. (2009) Kinetic evidence for interdomain communication in the allosteric regulation of α-isopropylmalate synthase from *Mycobacterium tuberculosis*. *Biochemistry* **48**, 1996–2004
26. Huisman, F. H., Squire, C. J., and Parker, E. J. (2013) Amino-acid substitutions at the domain interface affect substrate and allosteric inhibitor binding in α-isopropylmalate synthase from *Mycobacterium tuberculosis*. *Biochem. Biophys. Res. Commun.* **433**, 249–254
27. Frantom, P. A., Zhang, H. M., Emmett, M. R., Marshall, A. G., and Blanchard, J. S. (2009) Mapping of the allosteric network in the regulation of alpha-isopropylmalate synthase from *Mycobacterium tuberculosis* by the feedback inhibitor L-leucine: Solution-phase H/D exchange monitored by FT-ICR mass spectrometry. *Biochemistry* **48**, 7457–7464
28. Rambo, R. P., and Tainer, J. A. (2011) Characterizing flexible and intrinsically unstructured biological macromolecules by SAS using the Porod-Debye law. *Biopolymers* **95**, 559–571
29. Dalvit, C., Fogliatto, G., Stewart, A., Veronesi, M., and Stockman, B. (2001) WaterLOGSY as a method for primary NMR screening: practical aspects and range of applicability. *J. Biomol. NMR.* **21**, 349–359
30. Frantom, P. A. (2012) Structural and functional characterization of α-isopropylmalate synthase and citramalate synthase, members of the LeuA dimer superfamily. *Arch. Biochem. Biophys.* **519**, 202–209
31. Zhang, P., Ma, J., Zhang, Z., Zha, M., Xu, H., Zhao, G., *et al.* (2009) Molecular basis of the inhibitor selectivity and insights into the feedback inhibition mechanism of citramalate synthase from *Leptospira interrogans*. *Biochem. J.* **421**, 133–143
32. Ma, J., Zhang, P., Zhang, Z., Zha, M., Xu, H., Zhao, G., *et al.* (2008) Molecular basis of the substrate specificity and the catalytic mechanism of citramalate synthase from *Leptospira interrogans*. *Biochem. J.* **415**, 45–56
33. Bulfer, S. L., Scott, E. M., Pillus, L., and Trievel, R. C. (2010) Structural basis for L-lysine feedback inhibition of homocitrate synthase. *J. Biol. Chem.* **285**, 10446–10453
34. Feller, A., Ramos, F., Piérard, A., and Dubois, E. (1999) In *Saccharomyces cerevisae*, feedback inhibition of homocitrate synthase isoenzymes by lysine modulates the activation of LYS gene expression by Lys14p. *Eur. J. Biochem.* **261**, 163–170
35. Bulfer, S. L., Scott, E. M., Couture, J. F., Pillus, L., and Trievel, R. C. (2009) Crystal structure and functional analysis of homocitrate synthase, an essential enzyme in lysine biosynthesis. *J. Biol. Chem.* **284**, 35769–35780
36. Okada, T., Tomita, T., Wulandari, A. P., Kuzuyama, T., and Nishiyama, M. (2010) Mechanism of substrate recognition and insight into feedback inhibition of homocitrate synthase from *Thermus thermophilus*. *J. Biol. Chem.* **285**, 4195–4205
37. Suzuki, T., Tomita, T., Hirayama, K., Suzuki, M., Kuzuyama, T., and Nishiyama, M. (2021) Involvement of subdomain II in the recognition of acetyl-CoA revealed by the crystal structure of homocitrate synthase from *Sulfolobus acidocaldarius*. *FEBS J.* **288**, 1975–1988

38. Kirby, N., Boldeman, J. W., Gentle, I., and Cookson, D. (2007) Conceptual design of the small angle scattering beamline at the Australian synchrotron. *AIP Conf. Proc.* **879**, 887–889
39. Kirby, N. M., Mudie, S. T., Hawley, A. M., Cookson, D. J., Mertens, H. D. T., Cowieson, N., *et al.* (2013) A low-background-intensity focusing small-angle X-ray scattering undulator beamline. *J. Appl. Crystallogr.* **46**, 1670–1680
40. Ryan, T. M., Trewhella, J., Murphy, J. M., Keown, J. R., Casey, L., Pearce, F. G., *et al.* (2018) An optimized SEC-SAXS system enabling high X-ray dose for rapid SAXS assessment with correlated UV measurements for biomolecular structure analysis. *J. Appl. Crystallogr.* **51**, 97–111
41. Konarev, P. V., Volkov, V. V., Sokolova, A. V., Koch, M. H. J., and Svergun, D. I. (2003) Primus: a Windows PC-based system for small-angle scattering data analysis. *J. Appl. Crystallogr.* **36**, 1277–1282
42. Huang, R., and Leung, I. K. H. (2019) Protein-small molecule interactions by WaterLOGSY. *Meth. Enzymol.* **615**, 477–500
43. Fielding, L. (2003) NMR methods for the determination of protein-ligand dissociation constants. *Curr. Top. Med. Chem.* **3**, 39–53
44. Fielding, L. (2007) NMR methods for the determination of protein–ligand dissociation constants. *Prog. Nucl. Magn. Reson. Spectrosc.* **51**, 219–242
45. Williamson, M. P. (2013) Using chemical shift perturbation to characterise ligand binding. *Prog. Nucl. Magn. Reson. Spectrosc.* **73**, 1–16
46. Jacobson, M. P., Friesner, R. A., Xiang, Z., and Honig, B. (2002) On the role of the crystal environment in determining protein side-chain conformations. *J. Mol. Biol.* **320**, 597–608
47. Jacobson, M. P., Pincus, D. L., Rapp, C. S., Day, T. J., Honig, B., Shaw, D. E., *et al.* (2004) A hierarchical approach to all-atom protein loop prediction. *Proteins* **55**, 351–367
48. Vanommeslaeghe, K., Hatcher, E., Acharya, C., Kundu, S., Zhong, S., Shim, J., *et al.* (2010) CHARMM general force field: a force field for drug-like molecules compatible with the CHARMM all-atom additive biological force fields. *J. Comput. Chem.* **31**, 671–690
49. Vanommeslaeghe, K., and MacKerell, A. D., Jr. (2012) Automation of the CHARMM general force field (CGenFF) I: bond perception and atom typing. *J. Chem. Inf. Model.* **52**, 3144–3154
50. Vanommeslaeghe, K., Raman, E. P., and MacKerell, A. D., Jr. (2012) Automation of the CHARMM general force field (CGenFF) II: assignment of bonded parameters and partial atomic charges. *J. Chem. Inf. Model.* **52**, 3155–3168
51. Yu, W., He, X., Vanommeslaeghe, K., and MacKerell, A. D., Jr. (2012) Extension of the CHARMM general force field to sulfonyl-containing compounds and its utility in biomolecular simulations. *J. Comput. Chem.* **33**, 2451–2468
52. Mayne, C. G., Saam, J., Schulten, K., Tajkhorshid, E., and Gumbart, J. C. (2013) Rapid parameterization of small molecules using the Force Field Toolkit. *J. Comput. Chem.* **34**, 2757–2770
53. Huang, J., and MacKerell, A. D., Jr. (2013) CHARMM36 all-atom additive protein force field: validation based on comparison to NMR data. *J. Comput. Chem.* **34**, 2135–2145